



Structural, Optical, Morphological and Electrical Properties of Cu doped Calcium Stannate Nanoparticles for Electrochemical Performance

V. BALASUNDARAM^{1,†}, G. SIVAKUMAR^{2,*}, A. SARATHKUMAR^{1,†}, J. HENRY^{3,†} and K. MOHANRAJ^{4,†}

¹Department of Physics, Annamalai University, Chidambaram-608002, India

²Centralised Instrumentation and Service Laboratory, Department of Physics, Annamalai University, Chidambaram-608002, India

³Department of Physics, School of Engineering & Technology, Dhanalakshmi Srinivasan University, Tiruchirappalli-621112, India

⁴Department of Physics, School of Basic and Applied Science, Central University of Tamil Nadu, Thiruvarur-610005, India

*Corresponding author: E-mail: gskdopcisl@gmail.com

Received: 2 October 2023;

Accepted: 4 November 2023;

Published online: 31 December 2023;

AJC-21488

In this work, the co-precipitation method was adopted to synthesize Cu (0.01 M, 0.02 M and 0.03 M) doped CaSnO₃ nanoparticles and the structural, optical, morphological and electrochemical characterization were studied using XRD, FTIR, UV-visible, photoluminescence, SEM and cyclic voltammetry with electrochemical impedance analysis. It is observed from XRD patterns that the peaks shift towards higher angles attributed to the substitution of Cu²⁺ ions for Ca²⁺ ions and confirms the orthorhombic structure of Cu²⁺ doped CaSnO₃. The average crystallite size is found in the range of 40–49 nm after Cu doping. FTIR analysis also confirmed the Cu doping in to the CaSnO₃ nanoparticles by the presence of vibrational peaks at 698, 622 and 581 cm⁻¹ due to Cu-O stretching and the peak 483 cm⁻¹ due to Sn-O stretching vibration. The calculated band gap values were found to be 4.7, 4.8 and 4.9 eV for Cu doping. The photoluminescence (PL) emission study showed the light emission in the visible region and the SEM images indicate the well-formed cubed particles about < 2 μm. Specific capacitance values are highest for 0.02 M Cu doped CaSnO₃ at about 1694 F/g, compared to 572 F/g, 922 F/g and 1626 F/g for pure, 0.01 M and 0.03 M Cu doped CaSnO₃ particles, respectively, at a scan rate of 10 mV/s. Overall, these findings indicate that 0.02 M and 0.03 M Cu doped CaSnO₃ are the promising candidates for energy storage applications.

Keywords: CaSnO₃ nanoparticles, Co-precipitation, Cyclic voltammetry, Electrochemical impedance.

INTRODUCTION

Calcium stannate (CaSnO₃), a high band gap semiconductor with a band gap of ~ 4.7 eV is considered a highly diverse oxide owing to its unique structure, properties and multifunctional applications. These included optoelectronics, catalysis, sensors, photodetectors, phosphors, lithium-ion batteries and so forth light harvesting from oxygen vacancies and A- and B-site dopants in CaSnO₃ perovskite through efficient photon utilization and local site engineering [1]. CaSnO₃ exhibit number of defects such as antisites, Schottky, oxygen vacancies and are reported to have significant influence on its optical, catalytic, magnetic, and electrical properties [2]. Tran *et al.* [3] demonstrated a self-powered deep-UV (DUV) p-i-n photodetector consisting of CaSnO₃ thin film as an efficient DUV absorber via a low-temperature solution process. Wag *et al.* [4] made an attempt to design high-efficiency CaSnO₃ semiconductor

photocatalyst by a facile one-step molten salt method without adding a capping agent. Bhat & Tomar [5] reported Mn and Ce inclusion into the hydrothermally synthesized wide band gap CaSnO₃ perovskite and observed that the charge storing capacity improved with doping. Sumithra & Jaya [6] reported the systematic investigation of microstructure, optical and magnetic properties of Fe and Co doped CaSnO₃ nanostructures prepared by facile hydrothermal route. The magnetization behaviour was explained based on the F-centre exchange interactions mediated by oxygen vacancies. Ochoa-Muñoz *et al.* [7] synthesized several perovskite nanoparticles MSnO₃ (M = Ba, Zn, Ca) at low temperature in a controllable and reproducible using the polymer complex method. Gupta *et al.* [8] harnessed the full gamut of light emission from violet-blue to deep red originating from oxygen vacancies (OVs) in undoped CaSnO₃ and Eu@CaO₈ and Eu@SnO₆ sites in the doped CaSnO₃:Eu³⁺ (CSOE) perovskite.

Shaili *et al.* [9] reported the comprehensive study of the spray-coated CaSnO_3 thin films onto the Si (100) substrate. Electrical properties collected at room temperature revealed a growing conductivity upon doping ratio increase with a simultaneous enhancement in the carrier concentrations and mobility. Similarly, Xia *et al.* [10] attempted to obtain the pure-phase red-emission phosphors using $\text{Ca}_{2-x}\text{Eu}_x\text{Sn}_{1-y}\text{Y}_y\text{O}_4$ ($x = y = 0.01-0.05$) via the one-step solid-state reaction. Several other researchers synthesized the different types of alkaline stannate thin films using different techniques [11-16]. However, the majority of research primarily focuses on the applications of CaSnO_3 materials in phosphor-based light emitting materials, temperature sensing, battery electrode materials, photocatalytic applications, *etc.*, rather than in supercapacitors. It is motivated us to prepare divalent metal doped CaSnO_3 nanomaterials for supercapacitor applications. Hence in this investigation, CaSnO_3 nanomaterials and Cu doped CaSnO_3 nanomaterials prepared by co-precipitation method by varying three different Cu concentrations (0.1, 0.2 and 0.3 M) and studied the structural, optical, morphological and electrochemical applications.

EXPERIMENTAL

Calcium chloride (CaCl_2), tin chloride dihydrate ($\text{SnCl}_2 \cdot 2\text{H}_2\text{O}$), sodium hydroxide and copper(II) chloride hexahydrate ($\text{CuCl}_2 \cdot 6\text{H}_2\text{O}$) were used as precursor materials. For the synthesis of CaSnO_3 nanoparticles, CaCl_2 (0.1 M) and $\text{SnCl}_2 \cdot 2\text{H}_2\text{O}$ (0.05 M) were dissolved in deionized water separately to form a homogeneous solution under magnetic stirring. Then 2 M NaOH solution was dispersed with 40 mL of deionized water and stirred for 10 min followed by the addition of NaOH solution dropwise to maintain a pH of 12 while stirring at 60 °C for 45 min. The obtained product was then washed several times with distilled water and ethanol before being dried in a hot air oven at 80 °C for 3 h. The as-prepared samples were calcined for 6 h at different temperatures (800, 900 and 1000 °C) at a rate of 5 °C/min by using a muffle furnace. Similar procedure was adapted for different Cu doped CaSnO_3 nanoparticles with varying concentrations (0.01, 0.02 and 0.03 M) of CuCl_2 .

RESULTS AND DISCUSSION

XRD studies: Fig. 1 displays the X-ray diffraction (XRD) patterns of CaSnO_3 nanoparticles doped with varying concentrations of Cu^{2+} ions (0.01, 0.02 and 0.03 M). The XRD patterns of CaSnO_3 nanoparticle shows crystalline peaks at $2\theta = 32.08^\circ$ (121), 46.04° (040), 22.57° (020), 57.55° (042) and 56.60° (321) corresponds to orthorhombic CaSnO_3 as matched well with JCPDS card No. 77-1797, 31-0392. The XRD results revealed that the peaks for Cu doped CaSnO_3 at 0.01, 0.02 and 0.03 M concentrations have shifted towards the higher angles, which may be attributed to the substitution of Cu^{2+} ions for Ca^{2+} ions, driven by the smaller ionic radius of Cu^{2+} compared to Ca^{2+} . Additionally, the appearance of the new peaks in the XRD pattern confirm the successful doping of Cu ions into the structure. The XRD analysis further confirms the orthorhombic structure of Cu^{2+} doped CaSnO_3 . It is also evident that the most prominent peak for 0.01 M Cu^{2+} doping occurs at $2\theta = 33.07^\circ$, corresponding to the (121) plane. Other observable peaks are

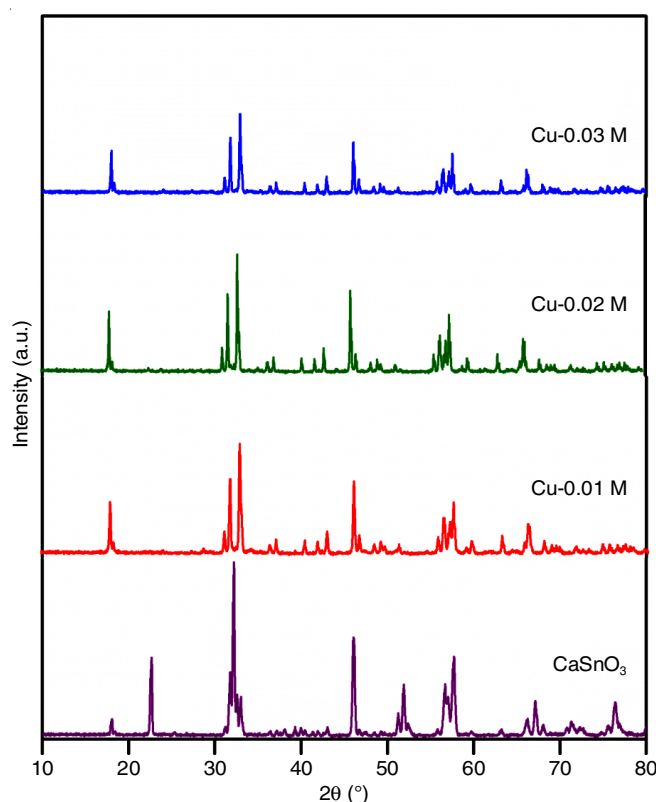
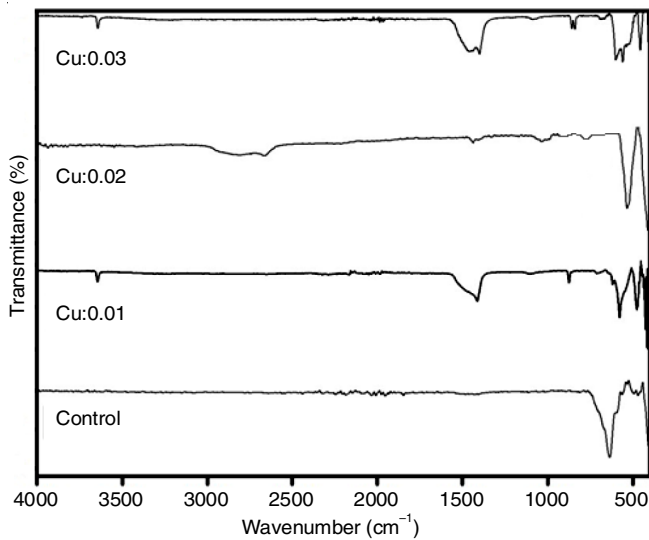


Fig. 1. XRD patterns of Cu doped CaSnO_3

located at $2\theta = 46.16^\circ$, 31.62° , 56.58° and 57.61° , corresponding to the (040), (200), (042) and (321) planes. The obtained peaks are well agreed with JCPDS card [31-0392]. The presence of Cu ions is confirmed by referencing the JCPDS cards [89-2531] and [89-5895]. The advantages of Cu are high electronic conduction, low cost, non-toxicity and chemical stability. However, the ionic radius of Cu is smaller than Ca and hence the crystalline peak broadens. For 0.02 M Cu^{2+} doping of CaSnO_3 , a predominant peak is observed at $2\theta = 32.87^\circ$, corresponding to the (121) plane. Some peaks are also observed at $2\theta = 45.90^\circ$, 31.64° , 57.46° and 33.07° , corresponding to the (040), (200), (042) and (210) planes. The crystallinity of the sample appears to decrease compared to undoped CaSnO_3 . The most prominent peak for 0.03 M Cu^{2+} doping is observed at $2\theta = 32.80^\circ$, corresponding to the (121) plane. Other peaks are identified at $2\theta = 46.20^\circ$, 31.99° , 57.53° and 33.22° , corresponding to the (040), (200), (042) and (210) planes. Similar to the 0.01 M Cu doped sample, the intensity of these crystalline peaks is reduced when compared to the undoped and 0.02 M Cu doped CaSnO_3 samples. The presence of Cu ions is verified using the JCPDS cards [89-2531] [15] and [89-5895] [16].

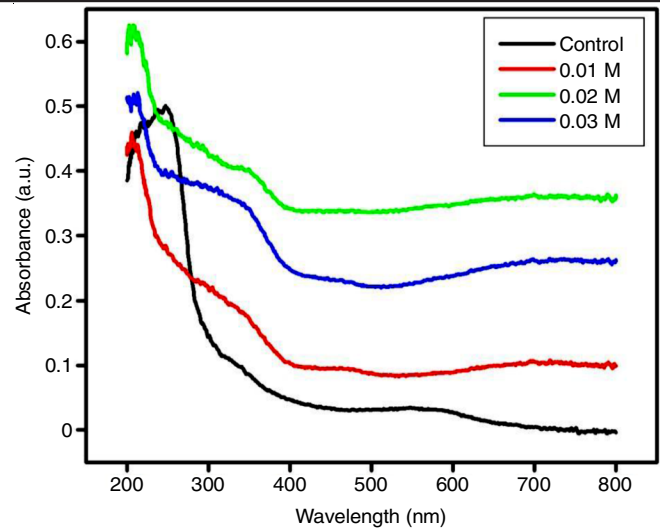
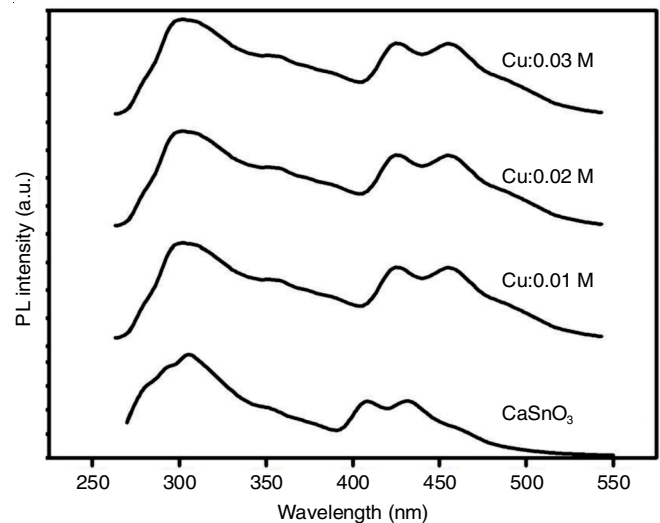
FTIR studies: In 0.01 M of Cu^{2+} doped CaSnO_3 , two peaks (Fig. 2) appear at 3641 cm^{-1} and 1412 cm^{-1} attributed to the Ca-O phase and bending vibration of the C-O bond [17]. The peaks at 1098 cm^{-1} and 876 cm^{-1} is assigned to carbonate vibration of Ca-O stretching [18,19]. The peak at 583 cm^{-1} is due to the presence of Cu-O stretching and it is important evidence for Cu^{2+} incorporation into the CaSnO_3 [20]. The peak 483 cm^{-1} is assigned to Sn-O stretching vibration [21].

Fig. 2. FTIR patterns of Cu doped CaSnO_3 nanoparticles

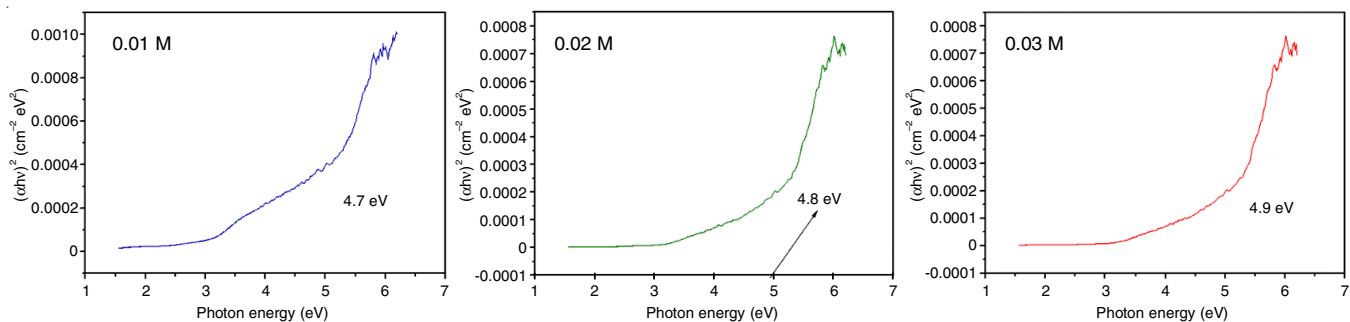
In the FTIR spectra of 0.02 and 0.03 M Cu doped CaSnO_3 , some peaks shown at 1489 and 1412 cm^{-1} due to the presence of stretching vibration of C-O bond [17]. The peak at 875 cm^{-1} is assigned to the Ca-O stretching [19]. The peaks at 698, 622 and 581 cm^{-1} are due to the presence of Cu-O stretching [19]. The peak at 474 cm^{-1} represents the Sn-O stretching [19]. The peak at 3642 cm^{-1} is observed which confirms the formation of the Ca-O phase [17]. The Cu incorporation is also confirmed by the Cu-O stretching vibration at 571 and 610 cm^{-1} [19].

UV-visible studies: Fig. 3 illustrates the UV-visible spectra of CaSnO_3 nanoparticles doped with three different concentrations of Cu. These prepared particles exhibit significant absorption in the UV region, with absorption peaks observed at 209, 206 and 214 nm for Cu^{2+} concentrations of 0.01, 0.02 and 0.03 M, respectively. An apparent shift to blue in the spectra is observed at all concentrations. The calculated bandgap values were 4.7, 4.8 and 4.9 eV for doping concentrations of 0.01, 0.02 and 0.03 M Cu, respectively (Fig. 4). These values represent an increase in the optical bandgap compared to undoped samples [22].

Photoluminescence (PL) studies: Fig. 5 illustrates the photoluminescence spectra of CaSnO_3 nanoparticles and Cu doped CaSnO_3 nanoparticles. The PL spectrum for CaSnO_3 was acquired with an excitation wavelength of approximately 245 nm. In case of pure CaSnO_3 , the PL emission occurs in the UV region at 307 nm is attributed to the intrinsic defects among

Fig. 3. UV absorption spectrum of Cu incorporated CaSnO_3 nanoparticlesFig. 5. PL emission spectra of Cu (0.01 M, 0.02 M, 0.03 M) incorporated CaSnO_3 nanoparticles

the constituents of CaSnO_3 matrix. Additionally, secondary emission peaks in the visible spectrum at 408 and 431 nm. The broad blue emission band spanning from 400 to 500 nm may result from defects, including oxygen vacancies, in the nanoparticles, with electronic energy levels situated below the 4f band [3]. In the PL spectrum of Cu doped CaSnO_3 with a concentration of 0.01 M, an emission band in the visible region

Fig. 4. Bandgap diagram of Cu doped CaSnO_3 nanoparticles

at 425 nm was observed accompanied by secondary peaks at 300 nm. While Cu doping, the blue emission peaks are shifted towards higher wavelength due to the charge transfer of Cu to the neighbouring oxygen atoms. As the Cu concentration is increased to 0.02 M, the emission peak shifts towards the 305 nm. The secondary peaks also get shifted towards higher wavelength and become apparent when excited at 248 nm. Finally at 0.03 M concentration, the emission peaks shift towards the

higher wavelength region with wavelengths of 460 nm observed under excitation at 329 nm. It is interesting to observe that the PL emission is constantly shifted towards the visible area when Cu is included into CaSnO_3 . The intensity of the Cu doped CaSnO_3 implies that the density of the defects increases with the Cu doping.

SEM studies: The SEM images (Fig. 6) represented the various concentration (0.01, 0.02 and 0.03 M) Cu doping CaSnO_3

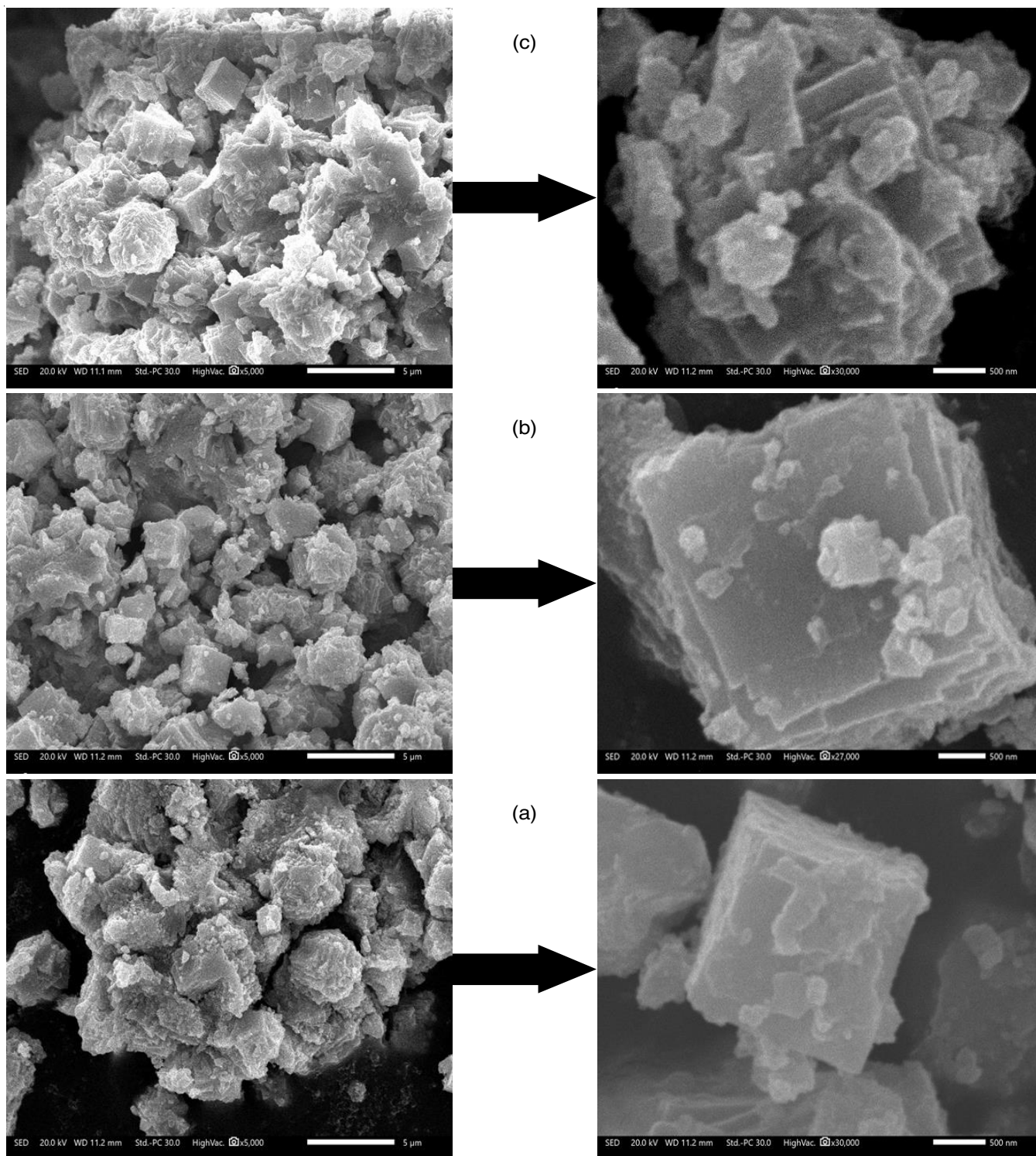


Fig. 6. SEM images of (a) 0.01 M, (b) 0.02 M and (c) 0.03 M Cu doped CaSnO_3 nanoparticles

nanoparticles. Formation of agglomerated cubic, spherical structure was observed in 0.01 M doped (Fig. 6a), whereas cubic nanoparticles ($< 2 \mu\text{m}$) are observed in 0.02 and 0.03 M Cu^{2+} doped CaSnO_3 nanoparticles. From its higher magnification, the crystallisation layer by layer formation is also observed. These particles are uniformly distributed across the surface, and their micro-cubic shapes are in accordance with the reported results [23].

Cyclic voltammetry: In Fig. 7, the CV measurements of synthesized pure CaSnO_3 and Cu doped CaSnO_3 nanoparticles are illustrated. As the scan rate increases, the peaks shift towards the higher potential regions and the integrated area of the CV curve increases. The areal capacitance (C_a) and specific capacitance (C_{sp}) values of CaSnO_3 electrode were determined using the appropriate equations [24,25]. The dynamic CV response of pure and Ce-doped CaSnO_3 nanoparticles is depicted in Fig. 7. In pure CaSnO_3 , a redox peak appears at -0.29 V during the anodic scan, while a distinct cathodic peak emerges at -0.63 V , possibly due to oxide layer thickening.

In case of Cu doping, redox peaks were observed at -0.12 V , -0.27 V and -0.08 V for 0.01 M, 0.02 M and 0.03 M, respectively. The shift in peaks towards higher potential regions may be attributed to material distortion, leading to electron transfer between redox-active species and the electrode surface. At low scan rates, sufficient interaction time between electrolyte ions and active electrode species leads to a higher probability of redox reactions. Conversely, at high scan rates, limited residence time restricts the interactions, resulting in fewer reactions at the electrode/electrolyte interface. Specific capacitance values are highest for 0.02 M Cu doped CaSnO_3 at about 1694 F/g , compared to 572 F/g , 522 F/g and 1626 F/g for pure, 0.01 M and 0.03 M Cu doped CaSnO_3 particles, respectively, at a scan rate of 10 mV/s . With increasing scan rates, the specific capacitance gradually decrease due to reduced integrated CV curve areas. The areal capacitance values were 26.1 F/g , 84.7 F/g and 80.08 F/g for 0.01 M, 0.02 M and 0.03 M Cu doped CaSnO_3 nanoparticles, respectively. It is also observed that the shape of cyclic voltammogram changes with varying Cu doping concentrations and among the electrodes, 0.02 M Cu doped CaSnO_3 stands out as a superior working electrode for supercapacitor applications. A higher specific capacitance (C_{sp}) values are observed for the sample 0.02 and 0.03 M Cu doped CaSnO_3 nanoparticles, which can be attributed to its small and uniform particles size as well as large surface area compared to pure

and another samples, which may leads to improved electrochemical properties.

The rectangular CV curve observed for CaSnO_3 indicates the efficient charge propagation within the synthesized materials. This phenomenon primarily stems from the charge and discharge processes associated with pseudocapacitive behaviour. Pseudocapacitors share the similarities with the electric double-layer capacitors (EDLCs) but differ in terms of their charge storage mechanism. Specifically, at low scan rates, the electrolyte ions have sufficient time to intercalate into the electrode material. In electrochemical measurements, the adsorption of ions predominates over the desorption of ions within the electrode/electrolyte system. Typically, adsorption-based supercapacitors exhibit the ability to provide higher specific capacitance, resulting in the characteristic rectangular CV curve. To achieve greater capacitance at lower scan rates and lower current densities, it is essential to maximize the number of active sites participating in the electrochemical reaction. The reason for the decrease in the specific capacitance values may be due to higher crystallite formed in the material during heat treatment. Theoretically, all the reactive sites involved in the electrochemical redox reactions need equal energy to participate in the reaction. But in practice, it is not equal and thus enables the electrochemical reactions to occur over a wide range of potential. To articulate the pseudocapacitive behaviour, the number of active sites involved in the electrochemical redox reaction.

To gain further insight into the electrochemical behaviour of the prepared electrodes, electrochemical impedance spectra (EIS) analyses were conducted. The Nyquist plot (Fig. 8) indicates a semi-circle region for all samples, representing the equivalent series resistance, which includes contact resistance and electrolyte resistance at the interface. The charge transfer resistance measured to be 0.979 , 1.70 and 10.5 for 0.01 M, 0.02 M, 0.03 M Cu^{2+} doped CaSnO_3 material, respectively. This lower resistance values compared to undoped CaSnO_3 particles may be attributed to a fast ion transfer mechanism and increased conductivity of CaSnO_3 nanoparticles. Overall, these findings indicate that 0.02 M and 0.03 M Cu^{2+} doped CaSnO_3 nanoparticles are the promising candidates for energy storage applications.

Conclusion

In this work, Cu (0.01, 0.02 and 0.03 M) doped CaSnO_3 nanoparticles synthesized by co-precipitation method and

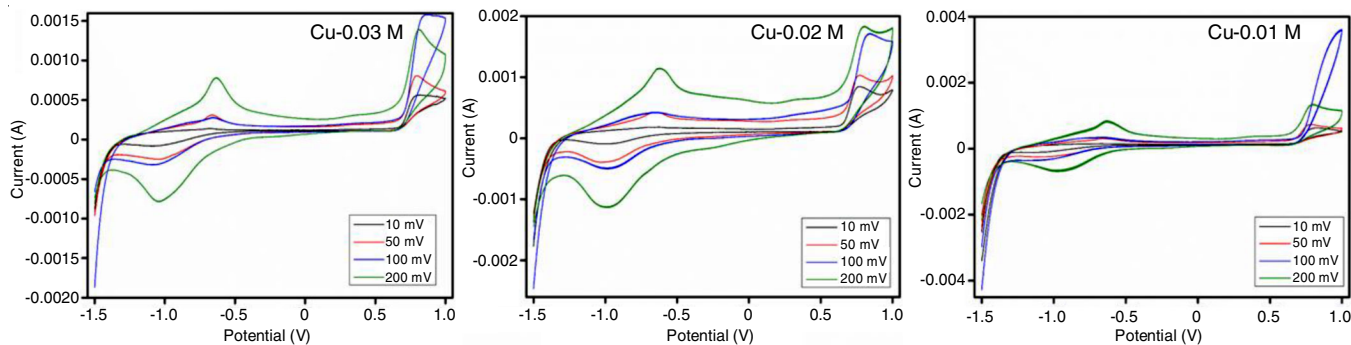


Fig. 7. CV plots of Cu doped CaSnO_3 particles

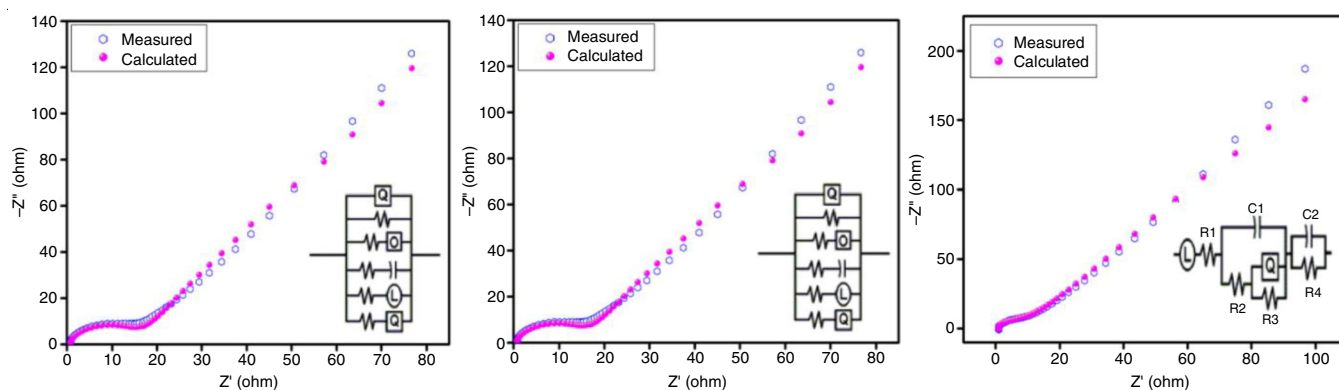


Fig. 8. Equivalent circuits of Cu doped CaSnO_3 particles

characterized. The XRD results revealed that the peaks shift towards higher angles attributed to the substitution of Cu^{2+} ions for Ca^{2+} ions, driven by the smaller ionic radius of Cu^{2+} compared to Ca^{2+} and confirmed the orthorhombic structure of Cu^{2+} doped CaSnO_3 nanoparticles. The average crystallite size was found to be 49.19, 40.30 and 40.92 nm, respectively for 0.01, 0.02 and 0.03 M Cu doping. FTIR analysis confirmed the Cu doping in to the CaSnO_3 nanoparticles by the presence of vibrational peaks at 698, 622 and 581 cm^{-1} due to Cu-O stretching and the peak 483 cm^{-1} due to Sn-O stretching vibration. The SEM analysis of 0.02 M and 0.03 M Cu^{2+} doped CaSnO_3 particles have cubic shaped particles about $< 2\ \mu\text{m}$. Specific capacitance values are highest for 0.02 M Cu doped CaSnO_3 at about 1694 F/g, compared to 572, 922 and 1626 F/g for pure, 0.01 M and 0.03 M Cu doped CaSnO_3 particles, respectively, at a scan rate of 10 mV/s. The charge transfer resistance is lowered about 0.979, 1.70 and 10.50 for 0.01 M, 0.02 M, 0.03 M Cu doped CaSnO_3 respectively compared to undoped CaSnO_3 particles which may be attributed to a fast ion transfer mechanism and increased conductivity of the CaSnO_3 nanoparticles.

CONFLICT OF INTEREST

The authors declare that there is no conflict of interests regarding the publication of this article.

REFERENCES

1. A. Novinrooz and P. Sarabadani, *Iran. J. Chem. Chem. Eng.*, **28**, 113 (2009); <https://doi.org/10.30492/IJCC.2009.13399>
2. Y. Liu, Y. Zhou, D. Jia, J. Zhao, B. Wang, Y. Cui, Q. Li and B. Liu, *J. Mater. Sci. Technol.*, **42**, 212 (2020); <https://doi.org/10.1016/j.jmst.2019.10.015>
3. M.H. Tran, T. Park and J. Hur, *ACS Appl. Mater. Interfaces*, **13**, 13372 (2021); <https://doi.org/10.1021/acsami.0c23032>
4. J. Wang, Y. Cui, Y. Xu, K. Xian, P. Bi, Z. Chen, K. Zhou, L. Ma, T. Zhang, Y. Yang, Y. Zu, H. Yao, X. Hao, L. Ye and J. Hou, *Adv. Mater.*, **34**, 2205009 (2022); <https://doi.org/10.1002/adma.202205009>
5. A.A. Bhat and R. Tomar, *J. Alloys Compd.*, **876**, 160043 (2021); <https://doi.org/10.1016/j.jallcom.2021.160043>
6. S. Sumithra and N.V. Jaya, *J. Mater. Sci. Mater. Electron.*, **29**, 4048 (2018); <https://doi.org/10.1007/s10854-017-8348-6>
7. Y.H. Ochoa-Muñoz, J.E. Rodríguez-Páez and R. Mejía de Gutiérrez, *Mater. Chem. Phys.*, **266**, 124557 (2021); <https://doi.org/10.1016/j.matchemphys.2021.124557>
8. S.K. Gupta, B. Modak, D. Das, A.K. Yadav, P. Modak, A.K. Debnath and K. Sudarshan, *ACS Appl. Electron. Mater.*, **3**, 3256 (2021); <https://doi.org/10.1021/acsaem.1c00426>
9. H. Shaili, E. Salmani, M. Beraich, M. Zidane, M. Taibi, M. Rouchdi, H. Ez-Zahraouy, N. Hassanain and A. Mzerd, *ACS Omega*, **6**, 32537 (2021); <https://doi.org/10.1021/acsomega.1c04054>
10. L. Xia, T. Hu, H. Liu, J. Xie, S.U. Asif, F. Xiong and W. Hu, *J. Alloys Compd.*, **845**, 156131 (2020); <https://doi.org/10.1016/j.jallcom.2020.156131>
11. S. Muraliedharan and A.M. Ashok, *Optik*, **287**, 171096 (2023); <https://doi.org/10.1016/j.ijleo.2023.171096>
12. Y. Hu, F. Zhou, X. Tian, C. Ji, Z. Huang, J. Wen, F. Luo, Z. Chen, X. Liu and Y. Peng, *Spectrochim. Acta A Mol. Biomol. Spectrosc.*, **243**, 118799 (2020); <https://doi.org/10.1016/j.saa.2020.118799>
13. T. Nakamura, M. Shima, M. Yasukawa and K. Ueda, *J. Sol-Gel Sci. Technol.*, **61**, 362 (2012); <https://doi.org/10.1007/s10971-011-2635-0>
14. B. Muthukutty, A. Krishnapandi, S.-M. Chen, M. Abinaya and A. Elangovan, *ACS Sustain. Chem. & Eng.*, **8**, 4419 (2020); <https://doi.org/10.1021/acssuschemeng.9b07011>
15. J. Wang, Y. Asakura, T. Hasegawa and S. Yin, *J. Environ. Chem. Eng.*, **10**, 108169 (2022); <https://doi.org/10.1016/j.jece.2022.108169>
16. G. Liu, Y. Li, J. Gao, D. Li, L. Yu, J. Dong, Y. Zhang, Y. Yan, B. Fan, X. Liu and L. Jin, *J. Alloys Compd.*, **826**, 154160 (2020); <https://doi.org/10.1016/j.jallcom.2020.154160>
17. P. Iniyavan, G.L. Balaji, S. Sarveswari and V. Vijayakumar, *Tetrahedron Lett.*, **56**, 5002 (2015); <https://doi.org/10.1016/j.tetlet.2015.07.016>
18. E. Hatzistavrou, X. Chatzistavrou, L. Papadopolou, N. Kantiranis, E. Kontonasi, A.R. Boccaccini and K.M. Paraskevopoulos, *Mater. Sci. Eng. C*, **30**, 497 (2010); <https://doi.org/10.1016/j.msec.2010.01.009>
19. V. Sumathi, R. Jayapragash, A. Bakshi and P. Kumar Akella, *Renew. Sustain. Energy Rev.*, **74**, 130 (2017); <https://doi.org/10.1016/j.rser.2017.02.013>
20. S. Srivastava, *IOSR J. Appl. Phys.*, **5**, 61 (2013); <https://doi.org/10.9790/4861-0546165>
21. H.Y. He, J. Fei and J. Lu, *J. Nanostruct.*, **5**, 169 (2015); <https://doi.org/10.1007/s40097-015-0147-0>
22. I.Z. Luna, L.N. Hilary, A.M.S. Chowdhury, M.A. Gafur, N. Khan, R.A. Khan, Bangladesh Atomic Energy Commission, *OALib*, **2**, 1 (2015); <https://doi.org/10.4236/oalib.1101409>
23. A. Sharma, P. Yadav, B. Khan, P. Kumar and M.K. Singh, *Mater. Today Proc.*, **82**, 308 (2023); <https://doi.org/10.1016/j.matpr.2023.02.007>
24. W. Zhang, J. Tang and J. Ye, *J. Mater. Res.*, **22**, 1859 (2007); <https://doi.org/10.1557/jmr.2007.0259>
25. F. Zhong, H. Zhuang, Q. Gu and J. Long, *RSC Adv.*, **6**, 42474 (2016); <https://doi.org/10.1039/C6RA05614H>